TASK QUARTERLY 7 No 2 (2003), 199–213

NUMERICAL SIMULATION AND MODIFICATION OF 3D FLOW PHENOMENA IN AN AXIAL FLOW FAN

EIMAD E. ELHADI AND WU KEQI

School of Energy and Power Engineering,
Huazhong University of Science and Technology,
Wuhan, 430074, P. R. China
mohandei@yahoo.com

(Received 6 October 2002; revised manuscript received 22 October 2002)

Abstract: This work aims to study and analyze the behavior of flow in an axial flow fan using numerical simulation based on solving Reynolds-averaged Navier-Stokes equations coupled with a modified Spalart-Allaras turbulence model. In the present work, different flow phenomena occuring in an axial flow fan were presented and interpreted at different design conditions and at different regions, with special concern to the rotor exit and stator regions. Large vortices and reverse flow at the stator suction side were observed under high loading conditions. These are mainly due to radial and centrifugal effects in the fluid due to a decreasing flow rate. To avoid this type of flow, the stator flow pattern has been modified using a new stator blade. This blade was designed by changing the stator stagger angle by 10° in the radial direction. This study indicates that the flow in the modified stator region behaves well and gives better performance than that obtained when using a baseline stator, especially under high loading conditions. This study also indicates that the stator stagger angle has a significant effect on modifying the fan performance.

Keywords: axial flow fan, vortex, stagger angle, numerical simulation, 3D

Nomenclature

u, v, w – velocity components
$\vec{E}$, $\vec{F}$, $\vec{G}$ – invicid flux vector
P_0 – total pressure
R – radial direction
$\vec{R}$, $\vec{S}$, $\vec{T}$ – viscous flow vector
Q – volume flow rate
D_t – diameter at tip of blade
U_t – peripheral speed of blade at tip (reference velocity)
T – torque
t – time
V_a – axial velocity
ρ – density
ω – angular velocity of rotor
η – total pressure efficiency
ν – hub/tip ratio

ϕ – flow coefficient
ψ – total pressure rise coefficient
τ_{ij} – viscous stress tensor
δ_{ij} – Kronecker-Delta

Subscript

1 – Inlet of the fan
2 – Outlet of the fan

Abbreviations

AVC – axial velocity coefficient
RPS – rotor pressure side
RSS – rotor suction side
SPS – stator pressure side
SSS – stator suction side
L.E. – leading edge

Definitions

$$AVC=\frac{V_a}{U_t} \qquad U_t=0.5D_t\omega \qquad \phi=\frac{Q}{\pi D_t^2(1-\nu^2)U_t/4} \qquad \psi=\frac{\Delta P}{\frac{1}{2}\rho U_t^2}$$

$$\eta=\frac{(P_{0_2}-P_{0_1})Q}{T\omega} \qquad \tau_{ij}=\mu\left(\frac{\partial u_i}{\partial x_j}+\frac{\partial u_j}{\partial x_i}\right)-\frac{2}{3}\mu\frac{\partial u_k}{\partial x_x}\delta_{ij} \qquad i,j,k=1,2,3$$

1. Introduction

Accurate and robust prediction of turbomachinery vortices flow and the study of their effects remains an objective of most research in the field of turbomachinery. Representation of flow in turbomachinery is difficult due to the existence of viscous wakes, secondary flow, turbulence, leakage flow and the interaction of different flows from these phenomena. Surely, turbomachinery internal flow analysis and design have benefited greatly from advance in computational power and efficiency. Denton [1] stated: "computational fluid dynamics (CFD) probably plays a greater part in the aerodynamic design of turbomachinery than it does in any other engineering application". Tallman [2] states: "CFD offers a tool for looking at the flow inside areas too small for measurements". He also stated that real engine parameters (*i.e.* physical geometry, boundary conditions, operating conditions and additional forces) could be modified much easier in a computational study.

In the present work, Reynolds-averaged Navier-Stokes equations, coupled with a modified Spalart-Allaras turbulence model, are solved numerically to analyze and discuss the generation and evolution of different vortices which occur inside an axial flow fan, with special concern to the flow in the stator region at different design conditions. In fact, there is little information in the available literature for the analysis of the stator region of axial flow fans. Most information is concerned with the rotor flow field region [3]. Accordingly, the present work aims to study the behavior of the axial flow fan with nine rotor blades and fifteen stator blades for the purpose of predicting high-vortex regions and suggesting further development of the considered fan to minimize such vortices.

In this study, axial flow fan blades were designed with a modified quasi-three dimensional code developed by the 2$^{\text{nd}}$ author (Wu Keqi, [4]) and widely used

in China. This code is based on solving the meridional flow using the streamline curvature theory and on selecting the blade element with NACA cascade data. Numerical simulation of the flow field of the fan was carried out using Reynolds-averaged Navier-Stokes equations coupled with a modified Spalart-Allmaras turbulent model for the purpose of closure.

2. Model of fan geometry

Calculations were carried out on an industrial axial flow fan (Figure 1) by the present numerical simulation.

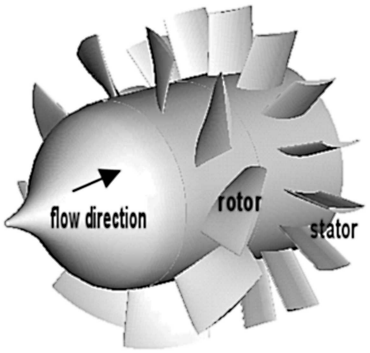

Figure 1. Axial flow fan configuration

The rotor and stator comprise of nine and fifteen blades respectively of standard NACA 65 series blade sections, and their aerodynamic design is such as to give a free vortex flow for the following design conditions:

Flow coefficient	0.415
Pressure rise coefficient	0.350
Hub/Tip ratio	0.600
Casing diameter	500 mm
Rotational speed	2200 rpm
Mach number	0.168

3. Governing equations

3.1. Navier-Stokes equations

These equations were employed in the following form:

$$\frac{\partial \vec{q}}{\partial t}+\frac{\partial \vec{E}}{\partial x}+\frac{\partial \vec{F}}{\partial y}+\frac{\partial \vec{G}}{\partial z}=\frac{\partial \vec{R}}{\partial x}+\frac{\partial \vec{S}}{\partial y}+\frac{\partial \vec{T}}{\partial z}, \tag{1}$$

where $\vec{q}=\begin{bmatrix}\rho\\ \rho u\\ \rho v\\ \rho w\end{bmatrix}$, $\vec{E}=\begin{bmatrix}\rho u\\ \rho u^2+p\\ \rho uv\\ \rho uw\end{bmatrix}$, $\vec{F}=\begin{bmatrix}\rho v\\ \rho uv\\ \rho v^2+p\\ \rho vw\end{bmatrix}$, $\vec{G}=\begin{bmatrix}\rho w\\ \rho uw\\ \rho vw\\ \rho w^2+p\end{bmatrix}$, $\vec{R}=\begin{bmatrix}0\\ \tau_{xx}\\ \tau_{xy}\\ \tau_{xz}\end{bmatrix}$,

$\vec{S}=\begin{bmatrix}0\\ \tau_{yx}\\ \tau_{yy}\\ \tau_{yz}\end{bmatrix}$, $\vec{T}=\begin{bmatrix}0\\ \tau_{zx}\\ \tau_{zy}\\ \tau_{zz}\end{bmatrix}$.

The first row of the above vector equations corresponds to the continuity equation; rows two, three and four are the momentum equations.

3.2. Turbulence model equations

Practically, the flow within turbomachines is turbulent. To capture the turbulence effect and reduce computational time, the grid is generated with high resolution and the Reynolds-averaged Navier-Stokes equations are solved. These equations have been easily derived by replacing μ with $(\mu+\mu_t)$, and velocity components and pressure – with their mean and disturbed values in Equation (1). Turbulent viscosity (μ_t) is determined by solving additional equations, which depend on the selected turbulence model [5]. The selection of a turbulence model depends on the type of grid, *i.e.* structured or unstructured grid [6]. Accordingly, for the present simulation the Spalart-Allaras turbulent model was used for the purpose of turbulence closure. This model is widely popular among CFD researchers. For more information about this model see [7] and [8].

4. Computational method

The present simulation used a numerical simulation based on a volume control technique to convert the governing equations to algebraic equations that can be solved numerically. The diffusion terms in the governing equations were discritized using second-order accurate central difference, while the convection terms were discritized using a second-order up-wind scheme. These equations were solved using an implicit segregated solver algorithm. This algorithm is based on solving the equations sequentially (*i.e.* segregated from one another). The SIMPLE algorithm method [9, 10] is used for the purposes of coupling between pressure and velocity and of satisfying the mass and momentum conservation laws. In order to check the convergence, the velocity components, and the kinetic energy and continuity of turbulence, residual values were calculated. The solution is said to be converging when each value of the previous residual is less than 10^{-5}.

5. Boundary conditions

A periodic boundary condition is used for all flow quantities at the blade-to-blade interface. For the purpose of generating high quality mesh, the computational domain was divided into two zones: one zone is the inlet and rotor region and the other is the stator and outlet region. The boundary plane between the two regions (especially between rotors and stators) is treated as the so-called mixing plane [11]. Atmospheric pressure and constant modified turbulence viscosity are prescribed at the inlet. The velocity components are defined at the outlet to consider different flow conditions.

6. Grid generation

As shown in Figure 2 and Table 1, the computational unstructured mesh used in the present simulation consists of two types of mesh which are: (a) quadrilaterals, which are used to mesh the rotor blade, the stator blade and the region surrounding the rotor and stator blades; (b) triangles, which are used to mesh the rest of the

domain. As also shown in Figure 2, the mesh is condensed at the rotor's leading edge so as to capture the most of the important flow field properties in these regions. As indicated by Sbardella [12] and verified by the present work, this type of grid has a high quality and good ability to predict most of the viscous flow phenomena.

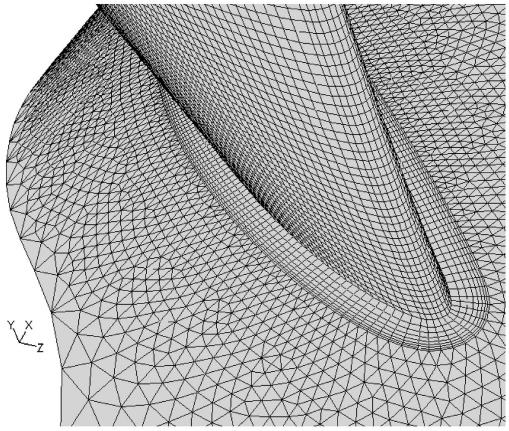

Figure 2. Sample of grid generation near rotor leading edge; the lower surface is the hub

Table 1. Number of grid points for basic surfaces.
Others-1 means: Inlet, outlet, periodic, surfaces at the mixing plane, inlet hub and inlet case. Others-2 means: rotor hub and case surfaces, stator hub and case surfaces. Mixed means: triangles and quadrilaterals were used. Total number of grids = 558320 grid points

Surface	Type of grid	Number of grid points
RPS	quadrilateral	152×100 in axial and span wise directions
RSS	quadrilateral	153×100 in axial and span wise directions
SPS	quadrilateral	91×100 in axial and span wise directions
SSS	quadrilateral	96×100 in axial and span wise directions
Others-1	triangles	7955
Others-2	mixed	27365

7. Results and discussion

In this work, to determine maximum vortices regions and analyze their effects on fan performance, sets of results were obtained as discussed below.

7.1. Determination of high-vortex regions

These regions can be determined by studying the meridional variations of the axial velocity coefficient (AVC), as shown in Figure 3. In this figure, stations 1 to 5 represent a rotor leading edge, a rotor trailing edge, the mixing plane's position, a stator leading edge and a stator trailing edge, respectively. These stations were taken at intersections of each edge with the hub. In fact, the existence of vortices or wake is indicated by a reduction in the axial velocity coefficient. As shown in

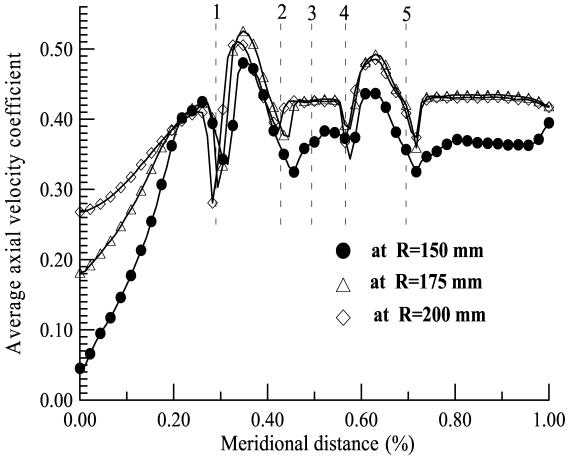

Figure 3. Meridional variations of average circumferential axial velocity coefficient at $\phi = 0.4145$

Figure 3, regions of greatly reduced axial velocity coefficient are located near the rotor and stator edges (leading and trailing edges). Reduction in the coefficient near the leading edge indicates the existence of either a horseshoe vortex or a leading edge vortex, which are largely affected by the radius of the leading edge, the sweep of the leading edge and rotational speed (in the case of a rotor). It is clearly visible from Figure 3 that maximum reduction of AVC at the leading edge for both the rotor and the stator is predicted near the hub, and the position of its minimum value moves toward the blade passage, due to the effect of hub, corner, or end wall vortices or their combined effects. A reduction in the axial velocity coefficient near the trailing edges indicates the existence of wake, a passage vortex or a combination of all vortices which occur up-stream of the trailing edge. As shown in Figure 3, the minimum of the axial velocity coefficient occurs near the hub at a position downstream of the trailing edge. Figure 3 also indicates uniform distribution of the axial velocity coefficient on both sides of the mixing plane except near the hub. This result ensures that the effect of rotor flow on stator flow is weak (which will be explained latter). Finally, Figure 3 reveals that the downstream flow at the stator exit is greatly affected by the hub, due to the relative motion between the hub (fixed) and the fluid flow in that region.

7.2. Flow at the rotor exit

Figure 4 is an axial velocity coefficient contour plot under design operating conditions. The free stream axial velocity is almost uniform, except near the hub, mainly due to the effect of the hub boundary layer. This result is clearly confirmed by Figure 5, which indicates a sudden reduction in axial velocity (large wake) near the hub in pitch position (-0.082m). It is apparent from these figures that the further away from the hub to mid span the lesser the reduction in axial velocity, and hence, wake becomes very weak.

7.3. Stator flow pattern

In order to study and analyze the flow in the stator region, different flow parameters, *i.e.* the static pressure coefficient, axial velocity, secondary flow and

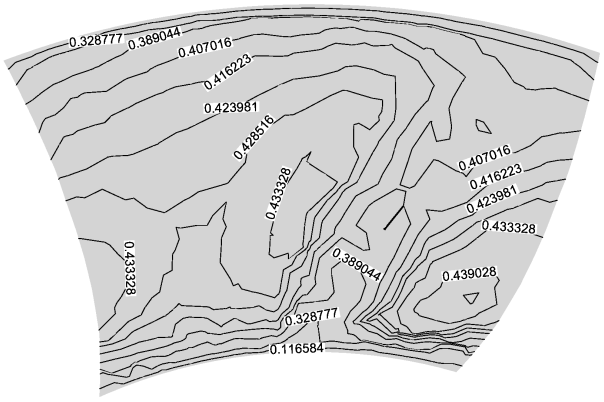

Figure 4. Contour of axial velocity coefficient behind a rotor at axial location 475mm

streamlines, were considered at two operating conditions and at different locations inside the stator flow pattern. Also, total pressure at the stator exit was considered under different loading conditions.

7.4. Stator flow pattern under design conditions

Figure 6 shows decrease in static pressure near the corner where a blade and the case intersect, due to the existence of a case boundary layer and a trailing edge vortex in that region. Yamamoto [13] found out that, for any strong vortex (passage), there is a minimum static pressure which nearly coincides with the vortex center. The vortex which occurs in this region can be clearly observed in Figure 7, which represents the secondary flow at the stator suction side under design conditions. The center of this vortex has been found to be about 5% span-wise from the case. Figure 7 also shows a small vortex flow at the hub near the stator trailing edge and smooth flow at other parts of the stator suction side. Note that in the present paper, to clearly see the existence of a vortex, the constant vector length theory was applied for all secondary vector plots.

7.5. Stator flow pattern under high loading conditions

Figure 8 indicates a sudden jump and reduction of static pressure near the stator hub at the suction side. This sudden change in pressure produces a vortex and reverse flows as shown in Figure 9. An early generation of a vortex and reverse flows have been shown in Figure 9. These flows grow larger and stronger and the flow characteristics of the stator's suction side becomes more complex due to the radial effect of the fluid which is produced as a result of a reduction in the flow rate [14].

7.6. Flow visualization in the stator flow region under various conditions

For the purpose of quantitative comparison between the stator flow pattern under various flow conditions, massless particle traces through the suction side were produced. These massless particles were released from the stator's leading edge. The predicted streamlines for design and high load conditions are shown in Figure 10.

For design conditions, Figure 10a shows a regular flow pattern at the stator's suction side, except near the upper corner at which the blade intersect with the case.

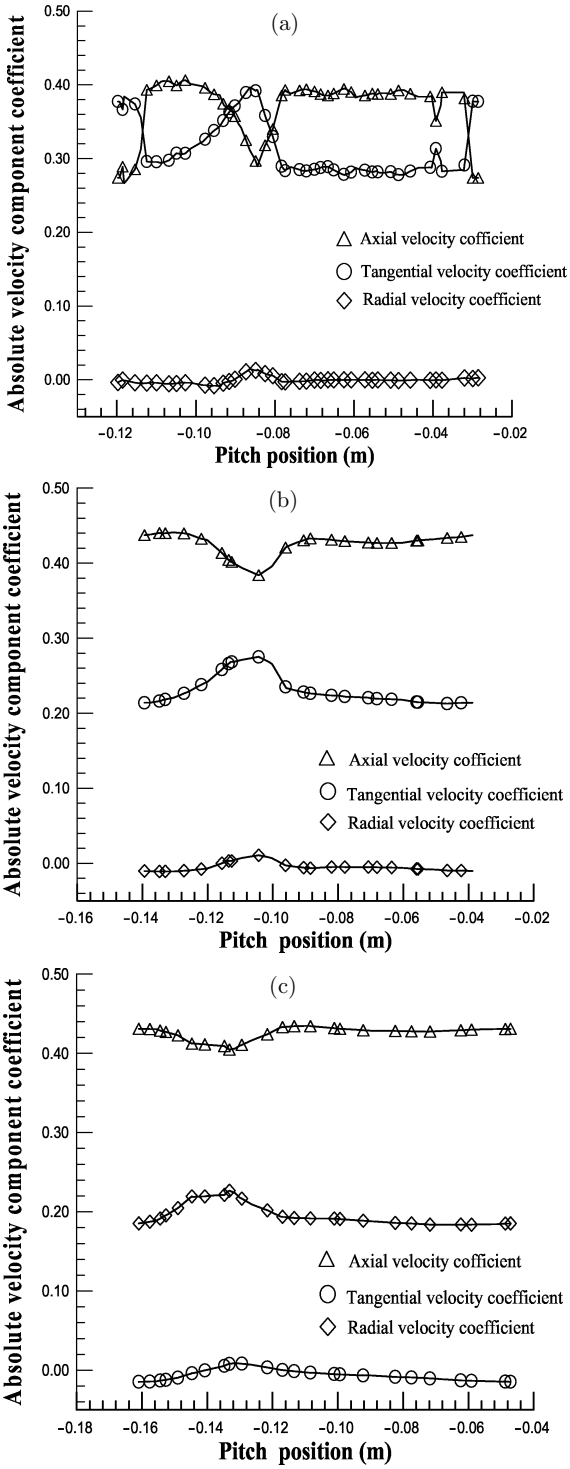

Figure 5. Pitch-wise variation of velocity components behind the rotor (at axial location = 475mm) for different radial locations: (a) near the hub ($R = 155$mm), (b) at $R = 175$mm, (c) at mid span ($R = 200$mm)

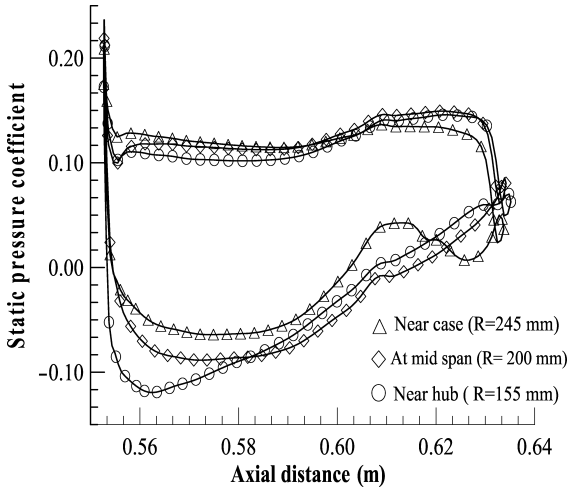

Figure 6. Stator surface static pressure distribution under design conditions ($\phi = 0.4145$)

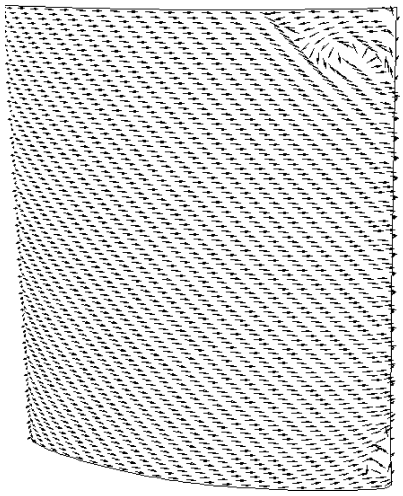

Figure 7. Secondary flow at the stator blade's suction side under design conditions

While Figure 10b indicates the existence of vortex flow near the hub up to about mid span and near the case down to about quarter span. From Figure 10b, one can infer the existence of a radial inflow near the case and the hub and a radial outflow near mid span, due to the reduction of flow rate.

7.7. Modification of stator flow pattern under high loading conditions

In the present work, for the purpose of modifying the stator flow pattern and hence the fan's performance, stator stagger angle has been increased by 10° in radial direction from the hub to the case. The modified stator configuration is referred to as stator (B) and the original one – as stator (A). These configurations are shown in Figure 11.

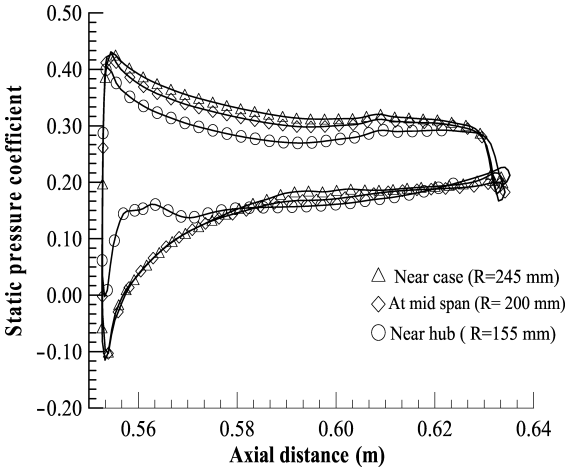

Figure 8. Stator surface static pressure distribution at $\phi = 0.332$

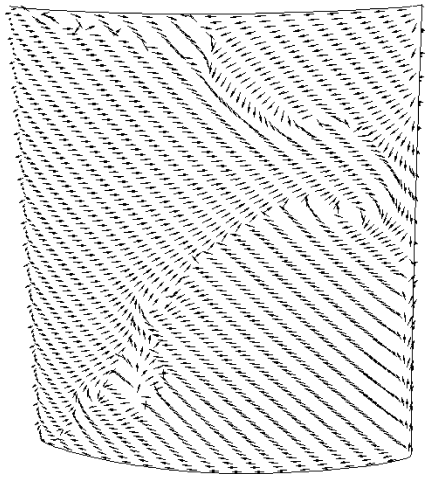

Figure 9. Secondary flow at the stator's suction side at $\phi = 0.332$

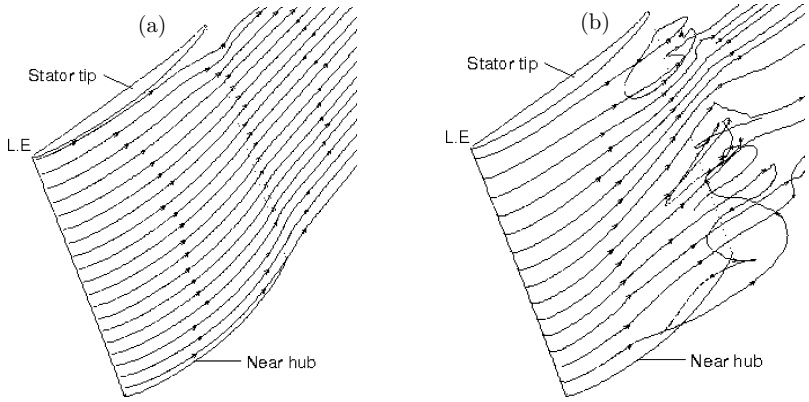

Figure 10. Streamlines flow pattern at the stator's suction side: (a) at $\phi = 0.4145$, (b) at $\phi = 0.332$

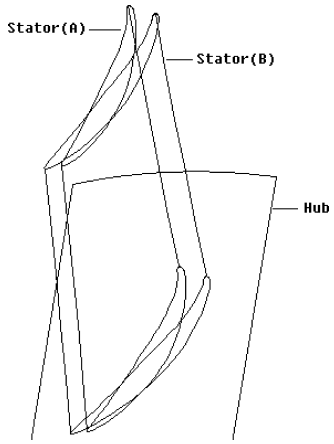

Figure 11. Stator (A) and stator (B)

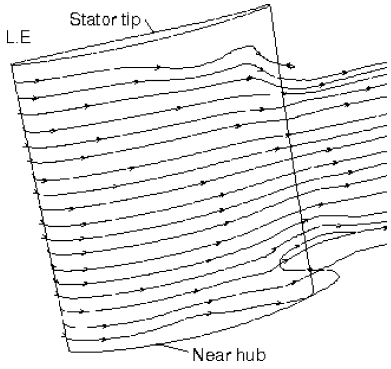

Figure 12. Streamlines flow pattern at stator (B)'s suction side ($\phi = 0.332$)

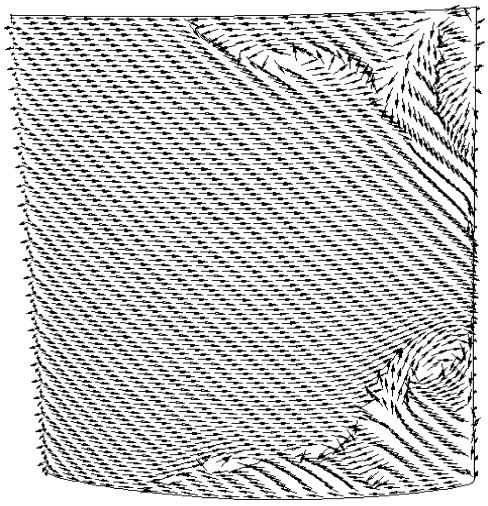

Figure 13. Secondary flow at stator (B)'s suction side ($\phi = 0.332$)

Figure 12 shows a reduction of vortices and reverse flow as compared with the original configuration (Figure 10b). This means that an increase in the stator stagger angle results in modifying the stator flow pattern. The modified flow can be clearly seen in Figure 13, which represents the secondary flow at stator (B)'s suction side under high loading conditions ($\phi = 0.332$). A vortex near the stator hub and case is visible there. It also shows that the flow away from the hub and the case is smooth and stable.

7.8. Flow field behind stator (A) and stator (B)

Figure 14 shows the variation of the axial velocity coefficient in the circumferential direction at different axial distances from the stator's trailing edge. It indicates the existence and decay of wake in the downstream region for both stator (A) and

stator (B). The figure also indicates the existence of weak wake in the case of stator (B), and that the flow in this case is more regular than when using stator (A), due to the effect of the increased stator stagger angle, which directly affects the behavior of the flow at the stator exit.

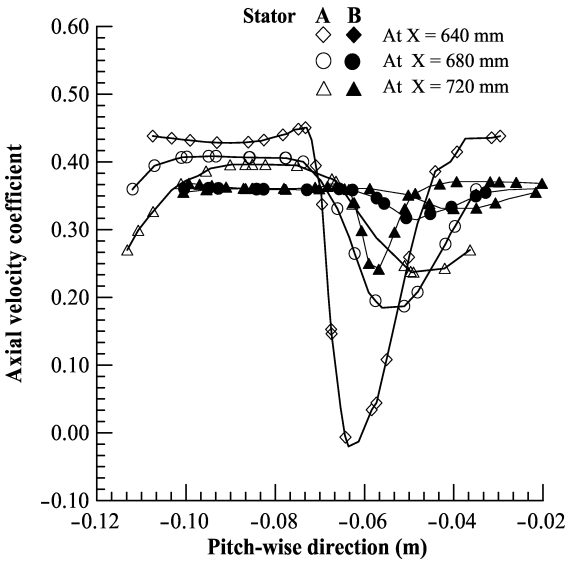

Figure 14. The axial velocity coefficient at the mid-span surface for various axial locations behind stator at $\phi = 0.332$

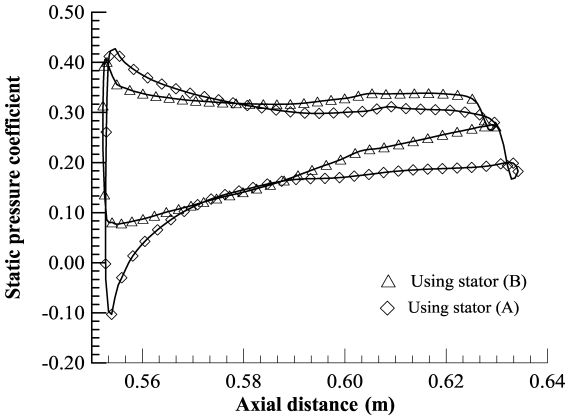

Figure 15. Surface static pressure distribution under high load conditions ($\phi = 0.332$) for stator (A) and stator (B)

7.9. Effect of stator stagger angle on axial fan performance

In fact, reduction in vortex flow results in modifying the performance of an axial flow fan. This can be clearly seen in Figures 15 and 16, which show an increase in static pressure when using stator (B). Figure 16b shows a weak reduction in static pressure behind stator (B) and more uniform static pressure distribution far from the stator exit, which results in weaker wake in the case of stator (B). The effect of

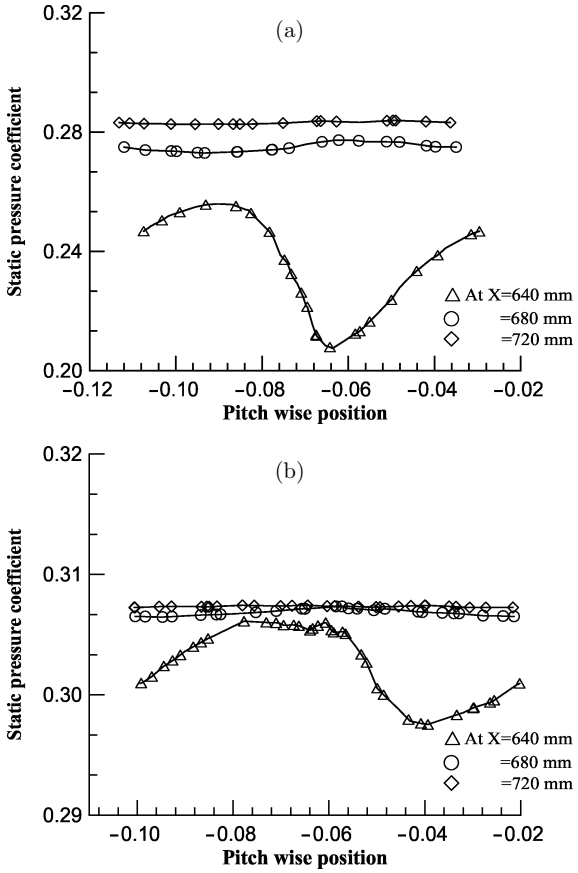

Figure 16. The static pressure coefficient at the mid-span surface for various axial locations behind (a) stator (A), (b) stator (B), at $\phi = 0.332$

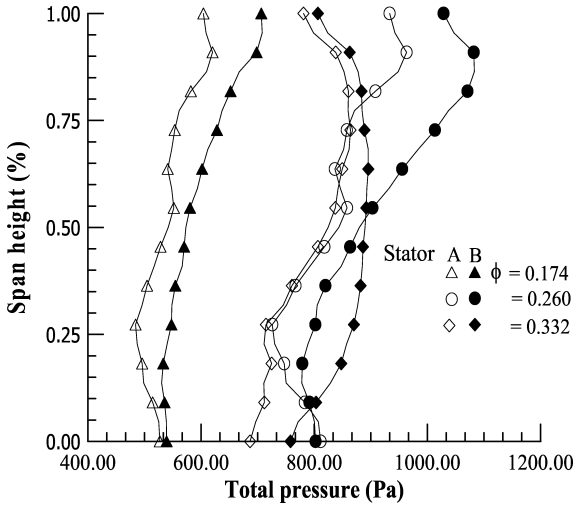

Figure 17. Radial distribution of average total pressure at the stator exit (≈ 35 mm from the trailing edge) under various loading conditions

the stator stagger angle on performance can be easily inferred from Figure 15, which indicates that stator (B) yields a greater total pressure rise than that produced when using stator (A) for all loading conditions. Figures 12 to 17 show that an increase in the stator stagger angle results in a reduction in the vortex, reverse flows and wake. It contributes to modify the performance of the fan, which clearly showed in increasing static pressure and total pressure in case of stator (B). For example, it has been found that an increase in the stator stagger angle by 10°, for $\phi = 0.332$, results in an increase in fan efficiency of 5.29% and an increase in the average total pressure at the outlet of the fan of 5.13%.

8. Conclusions

This paper gives details of flow behavior of different phenomena which occur at different regions inside an axial flow fan under various loading conditions. These were obtained by using a CFD code based on solving Reynolds-averaged Navier-Stokes equations coupled with a modified Spalart-Allaras turbulent model. The present paper investigates in detail the following aspects:

1. The characteristics of different vortices and wake meridionally at different radial positions. These characteristics curves are very useful to determine regions where vortices and wake exist.
2. The structure of flow behind the rotor. It has been found that wake decays downstream from rotor trailing edge until it reaches a certain position after which the wake becomes very weak.
3. Generation of vortices at the base line of stator (A)'s suction side under high loading conditions. As seen from the secondary flow, these vortices are born early near the stator's leading edge, which leads to a large reverse flow region at the stator's suction side.
4. The effect of the stator stagger angle on the behavior of flow and fan performance. It has been established that, the stator stagger angle has an effect on flow and hence on fan performance. As the stator stagger angle is increased by 10° in the radial direction, the flow behaves very well and good fan performance is obtained.

Acknowledgements

This study is supported by the National Science Foundation of China (no. 50176012).

References

[1] Denton J D and Dawes W N 1999 *J. Mech. Engng. Sci.* **C 213** (C2) 107
[2] Tallman J A 1999 *Simulation of Tip Leakage Flows in a Turbine Rotor using Computational Fluid Dynamics*, MSc Thesis in Mechanical Engineering, Pennsylvania State University
[3] Jens F, Sven B, Gunter K and Udo S 2001 *ASME J. Turbomachinery* **123** 483
[4] Keqi W and Inoure M 1984 *China-Japan Joint Conf. Hydraulic Machinery and Equipment*, Hangzhou, China, pp. 21–30
[5] Elhadi E E, Lie X and Keqi W 2002 *4th Int. Conf. Pumps and Fans*, Tsinghua University, Beijing, pp. 327–333
[6] Chunill H, FuLin T and James L 1998 *JSME Int. J., Series B* **41** (1) 200
[7] Dalcles J and Zilliac G G 1995 *AIAA J.* **33** (9) 1561

[8] Spalart P and Allmaras S 1992 *Technical Report, American Institute of Aeronautics and Astronautics*, AIAA-92-0439
[9] Pantankar S V 1972 *Int. J. Heat and Mass Transfer* **15** 1787
[10] Pantankar S V 1980 *Numerical Heat Transfer and Fluid Flow*, MC Graw-Hill
[11] Ruprecht A and Bauer C 1999 *ASME PVP Conference*, CFD Symposium, Boston, www.ihs.uni-stuttgart.de/forschung/veroeff/stroem/v1999_01.pdf
[12] Sbardella L and Imregun M 2001 *ASME, J. Turbomachinery* bf 123 568
[13] Yamamoto A and Nouse H 1988 *Effects of Incidence on Three Dimensional Flow in a Linear Turbine Cascade*, ASME88-GT-110
[14] Sabesky R H, Acosta A J and Hauptmann H 1971 *Fluid Flow*, 2nd Edition, New York, Macmillan